ACCOUNTS of chemical research

Article

pubs.acs.org/accounts

Computational Evaluation of Optoelectronic Properties for Organic/Carbon Materials

Zhigang Shuai,*[,†] Dong Wang,[†] Qian Peng,[‡] and Hua Geng[‡]

[†]Department of Chemistry and MOE Key Laboratory of Organic Optoelectronics and Molecular Engineering, Tsinghua University, Beijing 100084, China

[‡]Key Laboratory of Organic Solids and Beijing National Laboratory for Molecular Science, Institute of Chemistry, Chinese Academy of Sciences, Beijing 100190, China

CONSPECTUS: Organic optoelectronic materials are used in a variety of devices, including light-emitting diodes, field-effect transistors, photovoltaics, thermoelectrics, spintronics, and chemico- and biosensors. The processes that determine the intrinsic optoelectronic properties occur either in the photoexcited states or within the electron-pumped charged species, and computations that predict these optical and electrical properties would help researchers design new materials. In this Account, we describe recent advances in related density functional theory (DFT) methods and present case studies that examine the efficiency of light emission, carrier mobility, and thermoelectric figures of merit by calculation of the electron−vibration couplings.

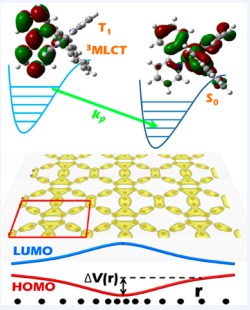

First we present a unified vibrational correlation function formalism to evaluate the excited-state radiative decay rate constant k_r, the nonradiative decay rate constant k_{nr}, the intersystem crossing rate constant k_{ISC}, and the optical spectra. The molecular parameters that appear in the formalism, such as the electronic excited-state energy, vibrational modes, and vibronic couplings, require extensive DFT calculations. We used experiments for anthracene at both low and ambient temperatures to benchmark the calculated photophysical parameters. In the framework of Fermi's golden rule, we incorporated the non-adiabatic coupling and the spin−orbit coupling to evaluate the phosphorescence efficiency and emission spectrum. Both of these are in good agreement with experimental results for anthracene and iridium compounds.

Band electron scattering and relaxation processes within Boltzmann theory can describe charge transport in two-dimensional carbon materials and closely packed organic solids. For simplicity, we considered only the acoustic phonon scattering as modeled by the deformation potential approximation coupled with extensive DFT calculations for band structures. We then related the carrier mobility to the band-edge shift associated with the lattice dilation of longitudinal waves. The calculated relaxation time was in good agreement with experimental data for the graphene sheet, which supports the methodology. We then found that the intrinsic electron mobility for a 6,6,12-graphyne sheet can be even larger than that of graphene.

We extended this approach to investigate the thermoelectric transport of electrons in metal phthalocyanines, which showed reasonable Seebeck coefficients when compared with experiments. For the thermal lattice transport, we employed nonequilibrium molecular dynamics simulations. Combining both electron transport and lattice thermal conductivity, we can evaluate the thermoelectric figure of merit.

1. INTRODUCTION

Molecular materials possess important application potential in optoelectronics. Organic light-emitting diodes (OLEDs) have been made highly efficient.[1] There has been great progress in organic field-effect transistors with high carrier mobility and on/off ratio as well as low threshold voltage.[2] With respect to energy applications, namely, organic photovoltaics[3] and thermoelectric conversion,[4] fast charge separation and transport as well as slow thermal transport are essential. We identify three key parameters to characterize the optoelectronic properties: the light-emitting quantum efficiency η, the carrier mobility μ, and the thermoelectric figure of merit zT. All of them are determined by the electronic−vibrational couplings, which can be assessed by density functional theory (DFT) and will be discussed in this Account.

The light-emitting quantum efficiency is expressed as $\eta = k_r/(k_r + k_{nr})$, where k_r is the radiative decay rate constant and k_{nr} is the nonradiative decay rate constant, representing internal conversion and intersystem crossing processes. For a two-level system, according to Einstein spontaneous emission we have $k_r = fE_g^2/1.499$, where f is the dimensionless oscillator strength and E_g is the energy gap in units of cm^{-1}, so that the k_r is expressed in units of s^{-1}. The value of k_r can be calculated even considering vibrational progressions and/or other complications such as Duschinsky rotation and Herzberg−Teller (HT) terms. However, the nonradiative decay, involving dissipation of electronic excitation into vibrational energy through non-adiabatic coupling and/or spin−orbit coupling, is much more complicated. We presented a rate formalism based on Fermi's golden rule (FGR) by following the early work of Huang and

Special Issue: DFT Elucidation of Materials Properties

Received: December 20, 2013
Published: April 4, 2014

   dx.doi.org/10.1021/ar400306k | Acc. Chem. Res. 2014, 47, 3301−3309

Rhys[5] and Lin,[6] which is exactly soluble when formulated in terms of the correlation function for two surfaces with displaced and distorted harmonic oscillators, containing parameters to be calculated by DFT.[7] Carrier mobility is one of the most important parameters governing the performance of an optoelectronic material. The intrinsic value is determined by the scattering of charge with lattice vibrations.[8] Regardless of whether the transport mechanism is hopping or bandlike, DFT-evaluated vibronic couplings are always essential.[9] For example, within the hopping model, the charge is trapped by intramolecular vibrations, and the charge reorganization energy can be regarded as the total relaxation energy of all the vibrational modes. For bandlike transport, the relaxation time for the charge distribution caused by scattering with phonons can be evaluated by DFT, and from it the electrical conductivity,[10] Seebeck coefficient,[11] and thermal conductivity[12] can be derived by virtue of the Boltzmann equation.

Thus, the evaluation of electron−phonon couplings is at the heart for both light emission and transport.[13] In the former case, the lowest electronic excited state along with the vibronic couplings can be evaluated with time-dependent DFT (TDDFT) in most cases. In the latter case, either the frontier-orbital state or the band-edge state is evaluated for its coupling with intramolecular vibration or the acoustic phonon as modeled by deformation potential (DP) theory for simplicity. In this Account, we present our combined approaches with DFT as the workhorse, aiming to predict the light-emitting efficiency, carrier mobility, and thermoelectric figure of merit for organic materials.

2. QUANTITATIVE PREDICTION OF LIGHT-EMITTING EFFICIENCY

The electronic excited state is short-lived and may undergo deactivation through a number of chemical and physical processes that result in either emission of light (luminescence) or nonradiative conversion of the excess energy into heat. The nonradiative decay of the lowest excited state to the ground state is a quantum dynamics problem for two potential energy surfaces[14,15] that is extremely difficult for large luminescent molecules with >50 atoms and long excited-state decay time scales of nanoseconds (fluorescence) to microseconds (phosphorescence). Recently, progress has been made in developing non-adiabatic dynamics methods including a surface-hopping algorithm[16] and excited-state molecular dynamics[17] to reveal the ultrafast relaxation process in complex systems. We opt for a harmonic oscillator model, which contains the quantum effect for the nuclear motion, which is often essential for optical transitions. In general, the two potential parabolas possess different equilibrium positions and shapes, and the kth normal coordinate of the initial state, Q_{ik}, can be expressed as a linear combination of all of the normal coordinates of the final state:[18]

$$Q_{ik} = \sum_{l=1}^{N} S_{i\leftarrow f,kl} Q_{fl} + D_{i\leftarrow f,k} \tag{1}$$

where $\mathbf{S}_{i\leftarrow f}$ is a unitary matrix, called the Duschinsky rotation matrix, whose elements represent the mixing of normal modes in the initial and final electronic states, and $\mathbf{D}_{i\leftarrow f}$ is a displacement vector connecting the minima of the parabolas of the two electronic states.

By virtue of FGR and second-order perturbation theory, the nonradiative decay rate constant is given by[19]

$$k_{nr} = \frac{2\pi}{\hbar} \sum_{\nu_i,\nu_f} P_{i\nu_i}(T) \left| \hat{H}'_{\nu_f,\nu_i} + \sum_{\nu_j} \frac{\hat{H}'_{\nu_f,\nu_j} \hat{H}'_{\nu_j,\nu_i}}{E_{i\nu_i} - E_{f\nu_f}} \right|^2 \delta(E_{i\nu_i} - E_{f\nu_f}) \tag{2}$$

where ν_i, ν_f, and ν_j are the vibrational quanta of the initial, final, and intermediate states, $P_{i\nu_i}(T)$ is the Boltzmann distribution of the vibrational manifolds in the initial state, and $\hat{H}'$ is the sum of the non-adiabatic coupling ($\hat{H}^{BO}$) and spin−orbit coupling ($\hat{H}^{SO}$) operators.

If the two states are in the same spin manifold, the spin−orbit coupling can be ignored, and only the first-order perturbation is considered. The internal conversion (IC) rate constant is then expressed as

$$k_{IC} = \frac{2\pi}{\hbar} \sum_{\nu_i,\nu_f} P_{i\nu_i}(T) \left| \sum_k \langle \Phi_f | \hat{P}_k | \Phi_i \rangle \langle \Theta_{f\nu_f} | \hat{P}_k | \Theta_{i\nu_i} \rangle \right|^2 \delta(E_{i\nu_i} - E_{f\nu_f}) \tag{3}$$

where $\hat{P}_k$ is the nuclear momentum operator for the kth mode and Φ and Θ are the electronic and vibrational state vectors, respectively. Equation 3 can be rewritten in a more compact form through Fourier transformation:

$$k_{IC} = \frac{1}{\hbar^2} \int_{-\infty}^{\infty} dt\ e^{i\omega_{if}t} \sum_{k,l} Z_i^{-1} \langle \Phi_f | \hat{P}_k | \Phi_i \rangle \langle \Phi_i | \hat{P}_l | \Phi_f \rangle \times \mathrm{Tr}[\hat{P}_k e^{-i\tau_f \hat{H}_f} \hat{P}_l e^{-i\tau_i \hat{H}_i}] \tag{4}$$

where Z_i is the partition function of the initial state, $\tau_i = -i\beta - t/\hbar$, $\tau_f = t/\hbar$, and $\hat{H}_i$ and $\hat{H}_f$ are the harmonic oscillator Hamiltonians of the initial and final states, respectively. It has been shown that the vibration correlation function Tr[...] in eq 4 can be solved by multidimensional Gaussian integrations,[20] and all of the quantities appearing in eq 4 can be calculated by DFT/TDDFT. The effect of Duschinky rotation on the internal conversion process was found to be essential for understanding aggregation-induced emission phenomena because mixing of low-frequency modes, which causes the density of states to spread out and thus enhances the IC rate, can be suppressed by aggregation.[18]

For nonradiative intersystem crossing (ISC) between different spin states, which combines the non-adiabatic coupling and spin−orbit coupling, eq 2 can be expanded into three terms, corresponding to $\hat{H}^{SO}$ only, the product of $\hat{H}^{SO}$ and $\hat{H}^{BO}$, and quadratic in $\hat{H}^{BO}$. Each term can be written as a time integration of vibrational correlation functions such as $\mathrm{Tr}[e^{-i\tau_f \hat{H}_f} e^{-i\tau_i \hat{H}_i}]$, $\mathrm{Tr}[\hat{P}_k e^{-i\tau_f \hat{H}_f} e^{-i\tau_i \hat{H}_i}]$, or $\mathrm{Tr}[\hat{P}_k e^{-i\tau_f \hat{H}_f} \hat{P}_l e^{-i\tau_i \hat{H}_i}]$ multiplied by the appropriate prefactors arising from the corresponding electronic couplings.[21]

For radiative processes, including optical absorption/emission spectra and decay rates, analogous vibrational correlation function formalisms that comprise both the Duschinsky rotation and HT effects can be obtained.[22] In this case, the electronic coupling term becomes the electric dipole moment $\boldsymbol{\mu}$. For the emission spectrum as an example, FGR gives

$$\sigma_{em}(\omega) = \frac{4\omega^3}{3\hbar c^3} \sum_{\nu_i,\nu_f} P_{i\nu_i} |\langle \Theta_{f\nu_f} | \hat{\boldsymbol{\mu}}_{fi} | \Theta_{i\nu_i} \rangle|^2 \delta(\omega_{i\nu_i,f\nu_f} - \omega) \tag{5}$$

Equation 5 can easily be recast into two parts: the transition dipole multiplied by a time integration over the correlation function $\mathrm{Tr}[e^{-i\tau_f \hat{H}_f} e^{-i\tau_i \hat{H}_i}]$ for the Franck−Condon term and

dx.doi.org/10.1021/ar400306k | Acc. Chem. Res. 2014, 47, 3301−3309

$\mathrm{Tr}[Q_k e^{-i\tau_f \hat{H}_f} e^{-i\tau_i \hat{H}_i}]$ and $\mathrm{Tr}[Q_k e^{-i\tau_f \hat{H}_f} Q_l e^{-i\tau_i \hat{H}_i}]$ for the HT terms. The optical absorption is obtained simply by exchanging the initial state and final state indices. The radiative decay rate constant is then found by integration over the emission spectrum: $k_r = \int_0^\infty \sigma_{em}(\omega)\, d\omega$.

For the radiative process, the transition dipole moments $\boldsymbol{\mu}_{fi}$ are easily obtained in TDDFT by tracing the transition density matrix $\boldsymbol{\xi}_{fi}$ with the electric dipole moment operator $\hat{\boldsymbol{\mu}}$: $\boldsymbol{\mu}_{fi} = \mathrm{Tr}(\hat{\boldsymbol{\mu}}\boldsymbol{\xi}_{fi})$. In this expression, ξ_{fi} is the solution to the TDDFT equation, given by

$$\xi_{fi}(x, x') = \sum_{i,a} [X_{ia}\varphi_a(x)\varphi_i(x') + Y_{ia}\varphi_i(x)\varphi_a(x')] \tag{6}$$

where as usual φ_i and φ_a are the occupied and virtual Kohn–Sham orbitals, respectively, and the transition density is $\rho_{fi} = \xi_{fi}(x, x)$. The first-order derivative of $\boldsymbol{\mu}_{fi}$ with respect to normal mode coordinate Q_k for the HT term, denoted as $\boldsymbol{\mu}_k$, is expressed as

$$\begin{aligned}\boldsymbol{\mu}_k &= \left(\frac{\partial \boldsymbol{\mu}_{fi}}{\partial Q_k}\right)_0 = e\left(\frac{\partial \int d^3x\, \rho_{fi}\mathbf{r}}{\partial Q_k}\right)_0 \\ &= e\int d^3x \left(\frac{\partial \rho_{fi}}{\partial Q_k}\right)_0 \mathbf{r} \\ &\equiv e\int d^3x\, \rho_k'\mathbf{r}\end{aligned} \tag{7}$$

The first-order non-adiabatic coupling between the ground and excited states in the framework of TDDFT has been developed and implemented by Send and Furche.[23] For coupling between any two excited states, only the multireference configuration interaction wave function method can be applied for the time being. The spin–orbit interaction operator can be approximated as

$$\hat{H}^{so} = \frac{e^2\hbar}{2m^2c^2}\left[\sum_{i,\sigma} Z_\sigma \mathbf{s}_i \cdot \left(\frac{\mathbf{r}_{i\sigma}}{r_{i\sigma}^3} \times \mathbf{p}_i\right) - \sum_{i\neq j}\left(\frac{\mathbf{r}_{ij}}{r_{ij}^3} \times \mathbf{p}_i\right)\cdot(\mathbf{s}_i + 2\mathbf{s}_j)\right] \tag{8}$$

Within the linear response theory, the transition moment between the ground state (0) and the excited state (f) is expressed as[24]

$$\langle 0|\hat{H}^{SO}|f\rangle = \lim_{\omega\to\omega_f} \hbar(\omega - \omega_f)\langle\langle \hat{H}^{SO}; V^{\omega_f}\rangle\rangle_\omega \tag{9}$$

where V^{ω_f} is the excitation vector. This expression can also be extended to transitions between two excited states from the double residues. For the dipole transition between different spin states, the quadratic response was developed by Tunell et al.[25] on the basis of TDDFT:

$$\boldsymbol{\mu}_{T_{1,\kappa}\to S_0} = \lim_{\omega_2\to\omega_T} (\omega_2 - \omega_T)\frac{\langle\langle \mathbf{r}; \hat{H}^{SO}, V^{\omega_2}\rangle\rangle_{0,\omega_2}}{\langle S_0|V^{\omega_2}|T_1\rangle} \tag{10}$$

As a benchmark for the combined methodology described above, we use the example of anthracene, for which well-established spectroscopic data are available for validation. We first performed equilibrium geometry optimizations and frequency and normal mode calculations for the S_0 and T_1 states by DFT and TDDFT, respectively. For the ISC process from S_1 to T_1/T_2, according to the second-order perturbation, intermediate states should be included that are coupled through non-adiabatic interactions, inducing the indirect spin–orbit coupling. Both the fluorescence and phosphorescence spectra were evaluated, and they are shown in Figure 1 in comparison with the experimental spectra. For better comparison, the spectra were calculated at different temperatures: absorption at 423 K, fluorescence at 433 K, and phosphorescence at 77 K. A Gaussian broadening of 10 cm^{-1} was employed for the phosphorescence spectrum to guarantee convergence of the time integration at low temperature. Furthermore, the calculated and experimental spectra were normalized to the maximal intensity, and the 0–0 transition energies were set to zero. The entire spectral shapes of the calculated spectra reproduce the experimental spectra well.[26,27] Especially, the hot bands below the 0–0 transition observed in the fluorescence measurement are fully reproduced.

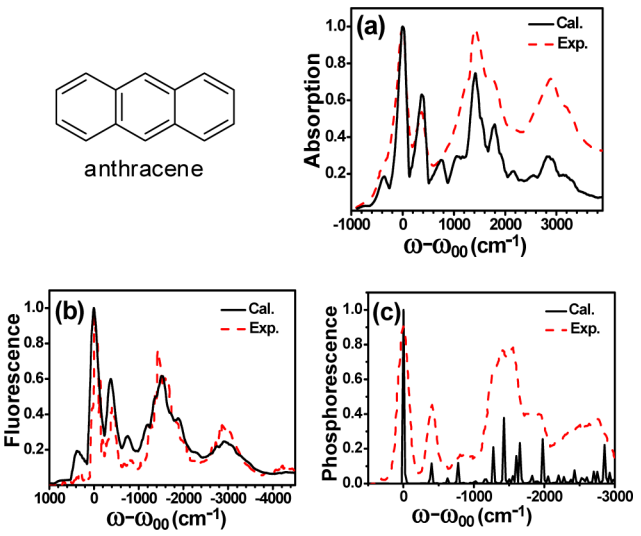

Figure 1. Comparisons of calculated and experimental spectra: (a) absorption at 423 K; (b) fluorescence at 433 K; (c) phosphorescence at 77 K.

Table 1 presents the calculated rate constants for the radiative decay and internal conversion from S_1 to S_0 and the intersystem crossing from S_1 to T_1/T_2 at room temperature, in comparison with the experimenal values. It is seen that (i) the calculated radiative and nonradiative decay rate constants are both in good agreement with experiment[29] and (ii) the rate constants for intersystem crossing from S_1 to T_1 and from S_1 to T_2 are 0.20×10^3 and 0.26×10^8 s^{-1}, respectively, in nice agreement with previous results.[30]

Table 1. Calculated Radiative, Internal Conversion, and Intersystem Crossing Rate Constants (unit: s^{-1}) of Anthracene at Room Temperature as well As the Corresponding Experiments

	k_r	k_{IC}	k_{ISC}	Φ_F
calc.	2.51×10^7	7.50×10^5	0.26×10^8	0.48
exp.	6.20×10^{7a}	3.5×10^{5a}	$(0.37\sim0.64) \times 10^{8b}$ 1.51×10^{8c}	0.29~0.62

[a]From ref 28. [b]From ref 29. [c]From ref 30.

Next we look at the iridium-based complexes, which have attracted great interest because of their potential applications in organic displays and solid-state lights. *fac*-Ir(ppy)$_3$ (ppy = 2-

dx.doi.org/10.1021/ar400306k | Acc. Chem. Res. 2014, 47, 3301–3309

phenylpyridine anion) is the most common green emitter, and its photophysical properties have been extensively studied both experimentally and theoretically.[31] The molecular phosphorescence is dictated by the lowest-lying excited triplet state, T_1. A triplet state consists of three substates, with zero-field splitting energies of ~100 cm^{-1} for the ^{3}MLCT states in organometallic compounds and about 0.1 cm^{-1} for the $^3\pi\pi^*$ states in pure organic compounds. *fac*-Ir(ppy)$_3$ has a zero-field splitting energy of about 83 cm^{-1}, exhibiting resolved features in the emission spectrum at temperatures below 25 K.[30] We take the average over these three substates at higher temperatures.

The geometry optimization and frequency calculations on the S_0 and T_1 states were performed using the CAM-B3LYP functional with the PVTZ basis sets for C, N, and H atoms and the LANL2DZ basis set for the iridium atom. First, we calculated the spectra at different temperatures (T = 77, 198, and 298 K) and compared them with the experimental spectra (Figure 2). Agreement between the calculated and experimental

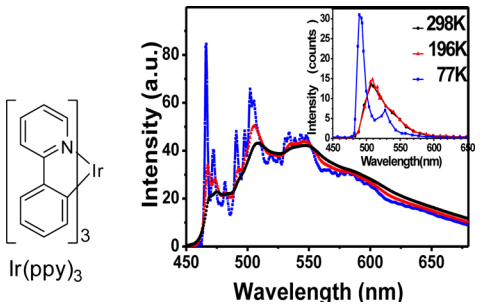

Figure 2. Comparison of the calculated and (inset) experimental phosphorescence spectra of *fac*-Ir(ppy)$_3$ at T = 77, 198, and 298 K.

spectra was found.[31]We then calculated the radiative rate constant, the rate constant for ISC from T_1 to S_0, and the phosphorescence quantum efficiency at room temperature for *fac*-Ir(ppy)$_3$. The calculated radiative decay rate constant is 6.36 × 10^5 s^{-1}, which is in good agreement with the experimental values of 5.6 × 10^5 s^{-1} in CH_2Cl_2 and 6.1 × 10^5 s^{-1} in 2-MeTHF.[32] Since the spin−orbit coupling matrix elements between S_0 and T_1 are 0.66, 0.91, and 133.61 cm^{-1} for the three substates in *fac*-Ir(ppy)$_3$, the first-order term in eq 2 is dominant and gives a rate constant of 5.04 × 10^4 s^{-1}, in good agreement with the experimental value (3.0 × 10^4 s^{-1}). Thereby, the phosphorescence quantum yield was predicted to be 92.7%, which lies within the experimentally measured range of 90−96% in different solutions at room temperature. The overall agreement demonstrates the predictive power of the present model and approach for OLED materials based on DFT/TDDFT-evaluated quantities.[33]

3. CHARGE AND THERMAL TRANSPORT IN ORGANIC SEMICONDUCTORS

Carrier mobility is the central parameter for optoelectronic materials. It describes the capacity for charges to move in the bulk material. In the presence of an external field F (e.g., an electric or magnetic field) or a thermal gradient, the charge acquires a momentum $\Delta q = mv$ that modifies the charge distribution. According to the classical Boltzmann transport theory, scattering tends to restore the momentum to the original value. Thus, for the steady state, under the relaxation time (τ) approximation, we have $mv = eF\tau$ or $v = (e\tau/m)F$, where τ originates from scattering with vibrations, impurities, and disorders. The charge mobility μ is then defined as the prefactor, that is, $\mu = e\tau/m$. This description is more appropriate for bandlike charge transport.[34]

3.1. Carrier Mobility of Carbon Nanomaterials

As far as intrinsic charge mobility is concerned, the phonon scattering mechanism should be considered. Since the de Broglie wavelength for an electron at 300 K corresponds to about 7 nm, which is much longer than the lattice spacing, we may consider only the acoustic phonon scattering at the long-wave limit, or the DP approximation.[35] Under such an assumption, the relaxation time is expressed as

$$\frac{1}{\tau_\alpha(i,\mathbf{k})} = \sum_{\mathbf{k}'\in \mathrm{BZ}} \left\{ \frac{2\pi}{\hbar} |M_i(\mathbf{k},\mathbf{k}')|^2 \delta[\varepsilon_i(\mathbf{k}) - \varepsilon_i(\mathbf{k}')] \times \left[1 - \frac{v_\alpha(i,\mathbf{k}')}{v_\alpha(i,\mathbf{k})}\right] \right\} \tag{12}$$

where $M_i(\mathbf{k},\mathbf{k}')$ is the matrix element for scattering from state $\mathbf{k}$ to state $\mathbf{k}'$ for an electron in the ith band, $\varepsilon_i(\mathbf{k})$ is the band dispersion, $\mathbf{v}(i,\mathbf{k}) = \nabla\varepsilon_i(\mathbf{k})/\hbar$ is the electron group velocity, and the sum runs over all vectors $\mathbf{k}'$ in the Brillouin zone (BZ). According to equipartition of energy, which gives an energy of $k_BT/2$ for the acoustic phonon, the vibrational amplitude can be derived, and the thermal average of the scattering matrix element can be obtained as

$$\langle |M_i(\mathbf{k},\mathbf{k}')|^2 \rangle = \frac{k_BT(E_1^i)^2}{C_\beta} \tag{13}$$

where C_β is the elastic constant along the β (phonon propagation) direction and E_1^i is the deformation potential for the ith band. Both can be evaluated by periodic DFT calculations: the former is obtained by a quadratic fit of the total energy of a unit cell with respect to lattice dilation, and the latter is the linear slope of the band-edge position with respect to lattice dilation: $E_1 = \Delta E/(\Delta l/l_0)$, where ΔE is the shift in the bottom position of the conduction band (CB) or the top position of the valence band (VB) with respect to the cell length dilation $\Delta l/l_0$. Then, according to the Boltzmann transport theory, the charge mobility for electrons (e) or holes (h) is expressed as

$$\mu_\alpha^{e(h)} = \frac{e}{k_BT} \frac{\sum_{i\in \mathrm{CB(VB)}} \int \tau_\alpha(i,\mathbf{k}) v_\alpha^2(i,\mathbf{k}) \exp\left[\mp \frac{\varepsilon_i(\mathbf{k})}{k_BT}\right] d\mathbf{k}}{\sum_{i\in \mathrm{CB(VB)}} \int \exp\left[\mp \frac{\varepsilon_i(\mathbf{k})}{k_BT}\right] d\mathbf{k}} \tag{14}$$

where the Fermi−Dirac distribution has been approximated by Boltzmann distribution for simplicity for large band gaps. It has been shown that for carbon nanomaterials, including graphene and graphynes, the acoustic-phonon scattering dominates over the optical-phonon scattering even at room temperature,[36] validating the DP approximation employed in our previous studies.[37−39]

Next we present one example of the prediction of the carrier mobility of a novel carbon nanomaterial, 6,6,12-graphyne,[40] a newly proposed sp−sp^2-hybridized two-dimensional (2D) carbon allotrope.[41] It has rectangular symmetry for the lattice structure and features Dirac cones in the band structure (Figure 3). 6,6,12-Graphyne is formed by partial insertion of carbon−carbon triple bonds into the carbon−carbon double bonds of

dx.doi.org/10.1021/ar400306k | Acc. Chem. Res. 2014, 47, 3301−3309

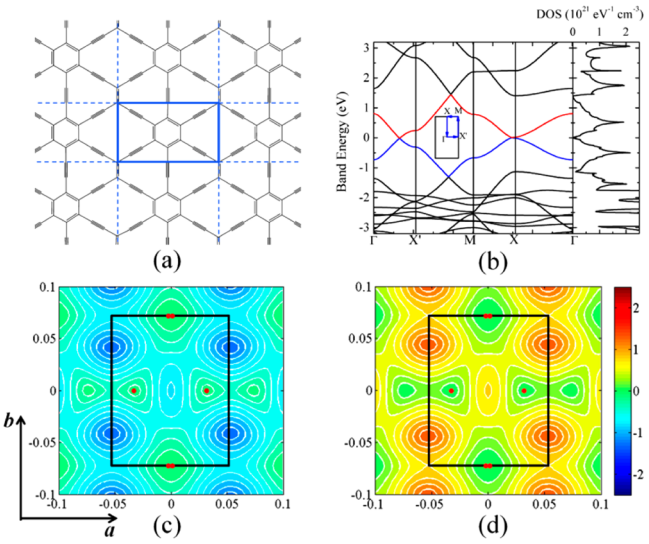

Figure 3. (a) Lattice structure, (b) band structure and densities of states (DOS), and (c, d) contour plots of the (c) valence band and (d) conduction band energies of 6,6,12-graphyne.

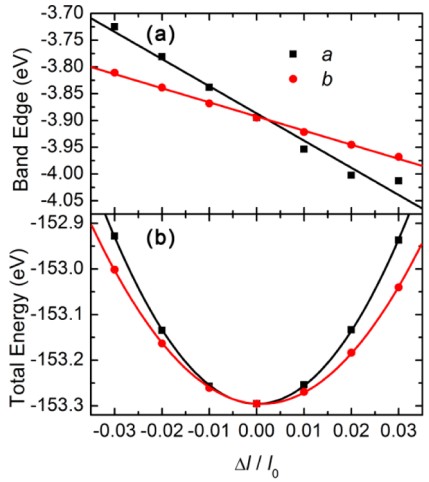

Figure 4. Band edge and unit cell total energy as functions of lattice dilation for 6,6,12-graphyne.

graphene, giving rise to an acetylenic linkage percentage of 41.67%. The lattice vectors and ionic positions were optimized with the projected augmented wave method and the Perdew–Burke–Ernzerhof (PBE) functional using the Vienna Ab Initio Simulation Package (VASP).[42] A 31 × 31 × 1 Monkhorst–Pack **k** mesh and an energy cutoff of 600 eV were applied. The optimized lattice constants were a = 9.44 Å and b = 6.90 Å. In contrast to graphene, which possesses one Dirac point at the K point, 6,6,12-graphyne exhibits two inequivalent Dirac points in the irreducible Brillouin zone. One is located along the high-symmetry line from Γ to X′ (denoted as Dirac cone I), and the other is located along the high-symmetry line from M to X close to the X point (denoted as Dirac cone II). Dirac cones I and II exhibit reflection symmetry about the mirror lines from Γ to X′ and M to X, respectively. The slope of Dirac cone I is apparently larger than that of Dirac cone II.

Since the 6,6,12-graphyne band features Dirac cones, the change in the Fermi level with dilation was followed. The DP constants obtained are 3.07 and 3.56 eV in the a and b directions, respectively, for both electrons and holes. With the same dilation scheme, the elastic constant C was obtained by a quadratic fit of the total energy E to the dilation $\Delta l/l_0$ as $(E - E_0)/S_0 = (C/2)(\Delta l/l_0)^2$, where S_0 is the unit cell area and E_0 is the total energy before dilation (Figure 4). The elastic constants are 99.37 and 50.52 J/m^2 in the a and b directions, respectively. Compared with graphene, 6,6,12-graphyne exhibits 2 times smaller elastic constants because of the much sparser carbon atoms and bond connections in its lattice. The DP constants of 6,6,12-graphyne are also smaller than those of graphene because the stronger triple bonds in the acetylenic linkages make the band energies less prone to change upon lattice deformation. The resulting relaxation times of 6,6,12-graphyne are 12.31 ps for holes and 17.75 ps for electrons in the a direction and 6.93 ps for holes and 9.99 ps for electrons in the b direction. We note that the relaxation time of electrons in 6,6,12-graphyne in the a direction is even larger than that in graphene (13.94 ps).

The band energies on a much finer 71 × 71 × 1 **k** mesh based on the previously converged charge density were calculated from non-self-consistent runs, and the accurate group velocities were obtained by the smoothed Fourier interpolation scheme proposed by Madsen and Singh,[43] which has been interfaced to VASP and our own code for relaxation times. The calculated intrinsic carrier mobilities for the 2D carbon materials are listed in Table 2, which shows that the electron mobility of 6,6,12-graphyne in the a direction was predicted to be even larger than that of graphene.

3.2. Evaluation of Charge Transport and Heat Transport: Prediction of Thermoelectric Figures of Merit

Thermoelectric materials interconvert heat and electricity via the Seebeck effect and the Peltier effect. The thermoelectric efficiency of a material is determined by its charge- and heat-transport properties. The methods to calculate carrier mobilities of nanomaterials described above can be easily extended to study the thermoelectric transport in closely packed molecular crystals or carbon materials showing bandlike transport behavior.

If a temperature gradient is applied to a material, a voltage gradient is created under the open-circuit condition, arising from heat-driven charge carrier diffusion from the hot junction to the cold junction. The phenomenon is known as the Seebeck effect. The Seebeck coefficient (S), also called the thermopower, is defined as the ratio of the voltage gradient to the temperature gradient. The electronic thermal conductivity (κ_e) is defined as the ratio of the heat current to the temperature gradient in the case of zero electrical current.

Within the framework of Boltzmann transport theory, the electrical conductivity (σ), the Seebeck coefficient, and the electronic thermal conductivity are all related to a kernel transport distribution function, defined as[44]

$$\sigma_{\alpha\beta}(\varepsilon) = \frac{e^2}{N}\sum_{i,\mathbf{k}} \tau(i,\mathbf{k})v_\alpha(i,\mathbf{k})v_\beta(i,\mathbf{k})\delta[\varepsilon - \varepsilon_i(\mathbf{k})] \quad (15)$$

The quantities in eq 15 are the same as in eq 14. By variation of the Fermi energy, carrier concentrations can be determined. The band structure is assumed to remain unchanged during doping, which is usually true at low carrier concentration when the host material is lightly doped. In the following, we illustrate the methodology and computational schemes by applying them to a metal phthalocyanine compound, TiOPc.[45]

The first-principles electronic structure calculations were based on the PBE functional. A 6 × 6 × 9 Monkhorst–Pack **k**

dx.doi.org/10.1021/ar400306k | Acc. Chem. Res. 2014, 47, 3301–3309

Table 2. Relaxation Times (τ) and Intrinsic Mobilities (μ) of Holes (h) and Electrons (e) at 300 K for α-Graphyne, β-Graphyne, 6,6,12-Graphyne, Graphene, and Graphdiyne

carbon allotrope	axis	τ^h (ps)	τ^e (ps)	μ^h (10^4 cm^2 V^{-1} s^{-1})	μ^e (10^4 cm^2 V^{-1} s^{-1})
α-graphyne	*a*	2.80	2.79	2.960	3.316
	b	2.84	2.83	2.716	3.327
β-graphyne	*a*	5.82	6.40	1.076	0.892
	b	5.37	5.91	0.856	0.798
6,6,12-graphyne	*a*	12.31	17.75	42.92	54.10
	b	6.93	9.99	12.29	24.48
graphene	*a*	13.80	13.94	32.17	33.89
	b	13.09	13.22	35.12	32.02
graphdiyne	*a*	1.94	19.11	1.97	20.81
	b	1.88	15.87	1.91	17.22

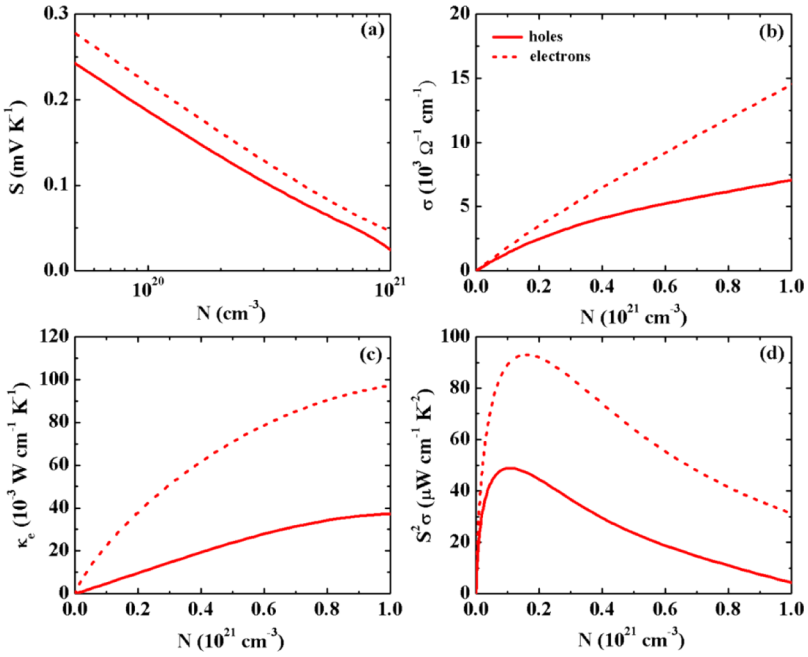

Figure 5. (a) Seebeck coefficient, (b) electrical conductivity, (c) electronic thermal conductivity, and (d) power factor of TiOPc in the *a* crystal direction as functions of the carrier concentration at room temperature. The Seebeck coefficient is negative for electrons, and the absolute value is shown here.

mesh was used for ionic relaxations. The band energies on a much denser 9 × 9 × 11 **k** mesh were obtained using the preconverged charge density, and then an interpolation scheme was followed to obtain accurate group velocities. The band gap of TiOPc was calculated to be 0.91 eV, which is typically underestimated, but it does not affect the computation of transport coefficients. The DP constants and the elastic constants were obtained from lattice dilations as described above for the mobility calculations of carbon nanomaterials. The DP constants were obtained as 1.75, 0.59, and 1.49 eV for holes and 0.02, 0.36, and 0.71 eV for electrons in the *a*, *b*, and *c* crystal directions, respectively. The elastic constants are 13.8 × 10^9, 14.0 × 10^9, and 10.1 × 10^9 J/m^3 in the *a*, *b*, and *c* directions, respectively. The scattering probabilities were averaged over the three crystal directions. The average relaxation times are 50.6 fs for electrons in the CB and 188.6 fs for holes in the VB.

The Seebeck coefficient is almost isotropic, shows maximum values of 1.38 mV/K for holes and 1.47 mV/K for electrons at zero carrier concentration, and decreases linearly with the logarithm of the carrier concentration (Figure 5). In the doping of organic semiconductors, the Seebeck coefficient is often measured, and it can be used to extract the carrier concentration in doped systems. When the carrier concentration is low, the electrical conductivity exhibits a linear relation with the carrier concentration, and the slope of the curve gives the carrier mobility of TiOPc. The obtained mobilities are 101, 20.6, and 16.6 cm^2 V^{-1} s^{-1} for holes and 123, 24.0, and 26.8 cm^2 V^{-1} s^{-1} for electrons in the *a*, *b*, and *c* crystal directions, respectively, at room temperature. The highest field-effect hole mobility reported for TiOPc thin films was 10 cm^2 V^{-1} s^{-1}.[46] This agreement between theory and experiment is reasonable considering the existence of grain boundaries in the polycrystalline thin films and other scattering mechanisms that were not taken into account in our calculations, including defect, impurity, and boundary scattering as well as optical-phonon scattering. The electronic thermal conductivity also increases linearly with the carrier concentration at low carrier concentration. The power factor, defined as $S^2\sigma$, exhibits a maximum value of 93.1 μW cm^{-1} K^{-2} for electrons at a certain carrier concentration and in the *a* direction.

dx.doi.org/10.1021/ar400306k | *Acc. Chem. Res.* 2014, 47, 3301−3309

To fully quantify the thermoelectric properties, the thermal conductivity contributed by lattice vibrations is needed. The lattice thermal conductivity (κ_L) in a perfect lattice arises from anharmonic lattice vibrations, which give rise to phonon−phonon scattering. The anharmonic lattice vibrations can be well-described by carefully parametrized classical force fields, which are usually obtained from fits to the first-principles-calculated structures and potential energies as well as the experimentally measured thermodynamic functions. We have shown that nonequilibrium molecular dynamics simulations with the general Amber force field can make reliable predictions of the lattice thermal conductivity of pentacene.[12] The predicted lattice thermal conductivity (0.61 W/mK) agrees well with the experimentally measured value (0.51 W/mK). Here we applied the same methodology to derive the lattice thermal conductivity of phthalocyanine.

The thermoelectric efficiency is quantified by the dimensionless thermoelectric figure of merit $zT = S^2\sigma/(\kappa_e + \kappa_L)$. With the transport coefficients of electrons and phonons determined, we can estimate the zT value for TiOPc as a function of carrier concentration (Figure 6). TiOPc exhibits a maximum zT value

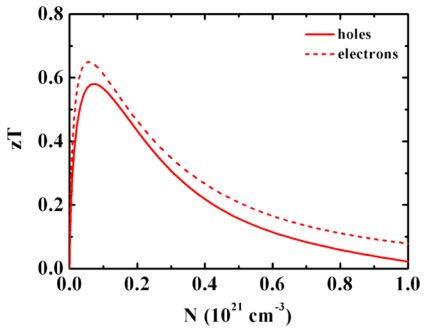

Figure 6. Figure of merit of TiOPc in the *a* direction as a function of carrier concentration at room temperature.

of 0.6 at a carrier concentration of 1.0×10^{20} cm^{-3} when it is n-doped. Accurate control of the dopant concentration and volume has been shown to be crucial for the optimization of the thermoelectric performance of PEDOT, which has a maximum zT of 0.42.[47] Our theoretical predictions could be helpful for screening and controlling the experimental conditions in the search for new organic thermoelectric materials.

4. CONCLUSION AND PERSPECTIVES

Chemistry is now much more focused on function than on structure. Computational chemistry has been following the trend or even leading the trend. The prediction of optoelectronic function, where electronic structure (especially the excited-state structure) and chemical dynamics (mostly electron dynamics) meet, is full of formidable challenges. Here we have presented a summary of methodological developments and computational studies on first-principles predictions of the light-emitting efficiency, charge carrier mobility, and thermoelectric figure of merit for organic materials with input from DFT calculations for the molecular parameters, such as the electronic excited state, vibrational modes, vibronic and nonadiabatic couplings, band structure and band-edge shift against lattice deformation, intermolecular electronic coupling, spin−orbit coupling, etc. This work is far from complete, since in principle the problem is essentially related to coupled electron and lattice quantum dynamics, at least at the nanosecond time scale. Nevertheless, using a harmonic model for two surfaces indeed works quantitatively well for both the light-emitting efficiency and spectra, partly because the optoelectronic properties do not involve any bond breaking or new bond formation, and thus, anharmonicity might be smeared out by the large number of degrees of freedom for our complex molecules containing up to 100 atoms, which are very different from diatomic molecules. Fermi's golden rule is a perturbation method that is valid only for weak couplings. To go beyond this approximation, surface hopping techniques as in non-adiabatic molecular dynamics are often applied.[16,17] As far as transport properties are concerned, the present deformation potential approach captures the feature of long coherence length of bandlike electrons, for which only scattering with acoustic phonons occurs. Reasonable results have been obtained for 2D carbon allotropes at room temperature. For more elaborate considerations, optical-phonon, boundary, and impurity scattering should be incorporated along with the charge localization effect caused by strong electron−phonon couplings, which is often described by a hopping model where charge delocalization is ignored.[48] A possible improvement in the calculation of electron−phonon couplings would be to include all phonon branches and dispersions on the basis of density functional perturbation theory.[49] Such computations are feasible by taking advantage of the localized Wannier functions for both electrons and phonons.[50] This field is full of challenges for future studies.

AUTHOR INFORMATION

Notes

The authors declare no competing financial interest.

Biographies

Zhigang Shuai received his B.Sc. in physics from Sun Yat-sen University in 1983 and his Ph.D. in theoretical physics from Fudan University in 1989. He accepted a full professor position under the "Hundred-Talent Program" in 2000 in the Institute of Chemistry of the Chinese Academy of Sciences in Beijing after working as research scientist for 11 years at the University of Mons, Belgium. He moved to Tsinghua University as a Changjiang Scholar Professor in 2008. His interests cover modeling of electronic processes in organic optoelectronic materials. He has been elected to the International Academy of Quantum Molecular Science, the Academy of Europe, and the Royal Academy of Belgium.

Dong Wang received her Ph.D. from the University of Science and Technology of China in 2000. She then worked as postdoc with Prof. Eitan Geva at the University of Michigan and with Prof. Gregory Voth at the University of Utah. She became an associate professor at Tsinghua University in 2010. Her research interests include theoretical investigation of thermoelectric organic materials and simulation of self-assembly phenomena.

Qian Peng received her Ph.D. from the Institute of Chemistry of the Chinese Academy of Sciences in 2008, supervised by Prof. Zhigang Shuai. Then she joined the Key Laboratory of Organic Solids in the Institute as a research assistant and was promoted to associate professor there in 2010. Her research interests are excited-state decay through non-adiabatic and spin−orbit couplings.

Hua Geng joined the Key Laboratory of Organic Solids at the Institute of Chemistry of the Chinese Academy of Sciences in 2003 as a research assistant to Prof. Zhigang Shuai. She received her Ph.D. from the Institute in 2011 and continues to work there. Her research

interests include theoretical modeling of charge transport in organic materials.

■ ACKNOWLEDGMENTS

This work was supported by the National Natural Science Foundation of China (Grants 21290191 and 91333202) and the Ministry of Science and Technology of China through the 973 Program (Grants 2011CB932304, 2011CB808405, and 2013CB933503).

■ REFERENCES

(1) Baldo, M. A.; Thompson, M. E.; Forrest, S. R. High-efficiency fluorescent organic light-emitting devices using a phosphorescent sensitizer. *Nature* **2000**, *403*, 750−753.
(2) Minemawari, H.; Yamada, T.; Matsui, H.; Tsutsumi, J. y.; Haas, S.; Chiba, R.; Kumai, R.; Hasegawa, T. Inkjet printing of single-crystal films. *Nature* **2011**, *475*, 364−367.
(3) Li, Y. F. Molecular design of photovoltaic materials for polymer solar cells: Toward suitable electron energy levels and broad absorption. *Acc. Chem. Res.* **2012**, *45*, 723−733.
(4) Sun, Y. M.; Sheng, P.; Di, C. A.; Jiao, F.; Xu, W.; Qiu, D.; Zhu, D. B. Organic thermoelectric materials and devices based on p- and n-type poly(metal 1,1,2,3-ethenetetrathiolate)s. *Adv. Mater.* **2012**, *24*, 932−937.
(5) Huang, K.; Rhys, A. Theory of light absorption and non-radiative transitions in F-centres. *Proc. R. Soc. London, Ser. A* **1950**, *204*, 406−423.
(6) Lin, S. H. Rate of interconversion of electronic and vibrational energy. *J. Chem. Phys.* **1966**, *44*, 3759−3767.
(7) Peng, Q.; Yi, Y. P.; Shuai, Z. G.; Shao, J. S. Excited state radiationless decay process with Duschinsky rotation effect: Formalism and implementation. *J. Chem. Phys.* **2007**, *136*, No. 114302.
(8) Shuai, Z. G.; Wang, L. J.; Li, Q. K. Evaluation of charge mobility in organic materials: From localized to delocalized descriptions at a first-principles level. *Adv. Mater.* **2011**, *23*, 1145−1153.
(9) Coropceanu, V.; Cornil, J.; da Silva Filho, D. A.; Olivier, Y.; Silbey, R.; Brédas, J.-L. Charge transport in organic semiconductors. *Chem. Rev.* **2007**, *107*, 926−952.
(10) Long, M. Q.; Tang, L.; Wang, D.; Wang, L. J.; Shuai, Z. G. Theoretical prediction of size-dependent carrier mobility and polarity in graphene. *J. Am. Chem. Soc.* **2009**, *131*, 17728−17729.
(11) Wang, D.; Tang, L.; Long, M. Q.; Shuai, Z. G. First-principles investigation of organic semiconductors for thermoelectric applications. *J. Chem. Phys.* **2009**, *131*, No. 224704.
(12) Wang, D.; Tang, L.; Long, M. Q.; Shuai, Z. G. Anisotropic thermal transport in organic molecular crystals from non-equilibrium molecular dynamics simulation. *J. Phys. Chem. C* **2011**, *115*, 5940−5946.
(13) Shuai, Z. G.; Xu, W.; Peng, Q.; Geng, H. From electronic excited state theory to the property predictions of organic optoelectronic materials. *Sci. China: Chem.* **2013**, *56*, 1277−1284.
(14) Lan, Z.; Fabiano, E.; Thiel, W. Photoinduced nonadiabatic dynamics of pyridine nucleobases: On-the-fly surface-hopping study with semiempirical methods. *J. Phys. Chem. B* **2009**, *113*, 3548−3555.
(15) Sun, X.; Miller, W. H. Semiclassical initial value representation for electronically non-adiabatic molecular dynamics. *J. Chem. Phys.* **1997**, *106*, 6346−6353.
(16) Akimov, A. V.; Neukirch, A. J.; Prezhdo, O. V. Theoretical insights into photoinduced charge transfer and catalysis at oxide interfaces. *Chem. Rev.* **2013**, *113*, 4496−4565.
(17) Nelson, T.; Fernandez-Alberti, S.; Chernyak, V.; Roitberg, A. E.; Tretiak, S. Non-adiabatic excited-state molecular dynamics modeling of photoinduced dynamics in conjugated molecules. *J. Phys. Chem. B* **2011**, *115*, 5402−5414.
(18) Peng, Q.; Yi, Y. P.; Shuai, Z. G.; Shao, J. S. Toward quantitative prediction of molecular luminescence quantum efficiency: Role of Duschinsky rotation. *J. Am. Chem. Soc.* **2007**, *129*, 9333−9339.
(19) Mebel, A. M.; Hayashi, M.; Liang, K. K.; Lin, S. H. Ab initio calculations of vibronic spectra and dynamics for small polyatomic molecules: Role of Duschinsky effect. *J. Phys. Chem. A* **1999**, *103*, 10674−10690.
(20) Ianconescu, R.; Pollak, E. Photoinduced cooling of polyatomic molecules in an electronically excited state in the presence of Duschinskii rotations. *J. Phys. Chem. A* **2004**, *108*, 7778−7784.
(21) Peng, Q.; Niu, Y. L.; Shi, Q. H.; Gao, X.; Shuai, Z. G. Correlation function formalism for triplet excited state decay: Combined spin−orbit and nonadiabatic couplings. *J. Chem. Theory Comput.* **2013**, *9*, 1132−1143.
(22) Niu, Y. L.; Peng, Q.; Deng, C. M.; Gao, X.; Shuai, Z. G. Theory of excited state decays and optical spectra: Application to polyatomic molecules. *J. Phys. Chem. A* **2010**, *114*, 7817−7831.
(23) Send, R.; Furche, F. First-order nonadiabatic couplings from time-dependent hybrid density functional response theory: Consistent formalism, implementation, and performance. *J. Chem. Phys.* **2010**, *132*, No. 044107.
(24) Ågren, H.; Vahtras, O.; Minaev, B. Response theory and calculations of spin−orbit coupling phenomena in molecules. *Adv. Quantum Chem.* **1996**, *27*, 71−92.
(25) Tunell, I.; Rinkevicius, Z.; Vahtras, O.; Salek, P.; Helgaker, T.; Ågren, H. Density functional theory of nonlinear triplet response properties with applications to phosphorescence. *J. Chem. Phys.* **2003**, *119*, 11024−11034.
(26) Ahn, T.-S.; Müller, A. M.; Al-Kaysi, R. O.; Spano, F. C.; Norton, J. E.; Beljonne, D.; Brédas, J.-L.; Bardeen, C. J. Experimental and theoretical study of temperature dependent exciton delocalization and relaxation in anthracene thin films. *J. Chem. Phys.* **2008**, *128*, No. 054505.
(27) Baba, M.; Saitoh, M.; Taguma, K.; Shinohara, K.; Yoshida, K.; Semba, Y.; Kasahara, S.; Nakayama, N.; Goto, H.; Ishimoto, T.; Nagashima, U. Structure and excited-state dynamics of anthracene: Ultrahigh-resolution spectroscopy and theoretical calculation. *J. Chem. Phys.* **2009**, *130*, No. 134315.
(28) Nijegorodov, N.; Ramachandran, V.; Winkoun, D. P. The dependence of the absorption and fluorescence parameters, the intersystem crossing and internal conversion rate constants on the number of rings in polyacene molecules. *Spectrochim. Acta Part A* **1997**, *53*, 1813−1824.
(29) Gastilovich, E.; Klimenko, V.; Korol Kova, N.; Nurmukhametov, R.; Serov, S. Effect of the vibronically induced spin-orbit coupling of electronic $\pi\pi^*$ states on nonradiative intersystem crossing: Anthracene. *Opt. Spectrosc.* **2008**, *105*, 38−45.
(30) Nijegorodov, N.; Vasilenko, V.; Monowe, P.; Masale, M. Systematic investigation of the influence of methyl groups upon fluorescence parameters and the intersystem crossing rate constant of aromatic molecles. *Spectrochim. Acta, Part A* **2009**, *74*, 188−194.
(31) Sajoto, T.; Djurovich, P. I.; Tamayo, A. B.; Oxgaard, J.; Goddard, W. A., III; Thompson, M. E. Temperature dependence of blue phosphorescent cyclometalated Ir(III) complexes. *J. Am. Chem. Soc.* **2009**, *131*, 9813−9822.
(32) Yersin, H.; Rausch, A. F.; Czerwieniec, R.; Hofbeck, T.; Fischer, T. The triplet state of organo-transition metal compounds. Triplet harvesting and singlet harvesting for efficient OLEDs. *Coord. Chem. Rev.* **2011**, *255*, 2622−2652.
(33) Shi, Q. H.; Peng, Q.; Sun, S. R.; Shuai, Z. G. Vibration correlation function investigation on the phosphorescence quantum efficiency and spectrum for blue phosphorescent Ir(III) complex. *Acta Chim. Sin.* **2013**, *71*, 884−891.
(34) Mahan, G. D. *Many-Particle Physics*, 3rd ed.; Kluwer Academic/Plenum: New York, 2000.
(35) Bardeen, J.; Shockley, W. Deformation potentials and mobilities in non-polar crystals. *Phys. Rev.* **1950**, *80*, 72−80.
(36) Borysenko, K. M.; Mullen, J. T.; Li, X.; Semenov, Y. G.; Zavada, J. M.; Nardelli, M. B.; Kim, K. W. Electron−phonon interactions in bilayer graphene. *Phys. Rev. B* **2011**, *83*, No. 161402.

(37) Long, M.; Tang, L.; Wang, D.; Li, Y.; Shuai, Z. Electronic structure and carrier mobility in graphdiyne sheet and nanoribbons: Theoretical predictions. *ACS Nano* **2011**, *5*, 2593−2600.
(38) Wang, D.; Shi, W.; Chen, J. M.; Xi, J. Y.; Shuai, Z. G. Modeling thermoelectric transport in organic materials. *Phys. Chem. Chem. Phys.* **2012**, *14*, 16505−16520.
(39) Xi, J.; Long, M.; Tang, L.; Wang, D.; Shuai, Z. First-principles prediction of charge mobility in carbon and organic nanomaterials. *Nanoscale* **2012**, *4*, 4348−4369.
(40) Chen, J.; Xi, J.; Wang, D.; Shuai, Z. Carrier mobility in graphyne should be even larger than that in graphene: A theoretical prediction. *J. Phys. Chem. Lett.* **2013**, *4*, 1443−1448.
(41) Malko, D.; Neiss, C.; Viñes, F.; Görling, A. Competition for graphene: Graphynes with direction-dependent Dirac cones. *Phys. Rev. Lett.* **2012**, *108*, No. 086804.
(42) Kresse, G.; Furthmüller, J. Efficient iterative schemes for ab initio total-energy calculations using a plane-wave basis set. *Phys. Rev. B* **1996**, *54*, 11169−11186.
(43) Madsen, G. K. H.; Singh, D. J. BoltzTraP: A code for calculating band-structure dependent quantities. *Comput. Phys. Commun.* **2006**, *175*, 67−71.
(44) Scheidemantel, T. J.; Ambrosch-Draxl, C.; Thonhauser, T.; Badding, J. V.; Sofo, J. O. Transport coefficients from first-principles calculations. *Phys. Rev. B* **2003**, *68*, No. 125210.
(45) Chen, J.; Wang, D.; Shuai, Z. First-principles predictions of thermoelectric figure of merit for organic materials: Deformation potential approximation. *J. Chem. Theory Comput.* **2012**, *8*, 3338−3347.
(46) Li, L.; Tang, Q.; Li, H.; Yang, X.; Hu, W.; Song, Y.; Shuai, Z.; Xu, W.; Liu, Y.; Zhu, D. An ultra closely π-stacked organic semiconductor for high performance field-effect transistors. *Adv. Mater.* **2007**, *19*, 2613−2617.
(47) Bubnova, O.; Khan, Z. U.; Malti, A.; Braun, S.; Fahlman, M.; Berggren, M.; Crispin, X. Optimization of the thermoelectric figure of merit in the conducting polymer poly(3,4-ethylenedioxythiophene). *Nat. Mater.* **2011**, *10*, 429−433.
(48) Geng, H.; Peng, Q.; Wang, L. J.; Li, H. J.; Liao, Y.; Ma, Z. Y.; Shuai, Z. G. Towards quantitative prediction of charge mobility in organic semiconductors: Tunneling enabled hopping model. *Adv. Mater.* **2012**, *24*, 3568−3572.
(49) Baroni, S.; de Gironcoli, S.; Dal Corso, A.; Giannozzi, P. Phonons and related crystal properties from density-functional perturbation theory. *Rev. Mod. Phys.* **2001**, *73*, 515−562.
(50) Giustino, F.; Cohen, M. L.; Louie, S. G. Electron−phonon interactions using Wannier functions. *Phys. Rev. B* **2007**, *76*, No. 165108.